Draft version December 22, 2014
Preprint typeset using LaTeX style emulateapj v. 12/16/11

TICK TOCK: *MOST* TIMES THE MAGNETOSPHERIC CLOCK OF σ ORI E

R. H. D. Townsend[1], Th. Rivinius[2], J. F. Rowe[3], A. F. J. Moffat[4], J. M. Matthews[5], D. Bohlender[6], C. Neiner[7], J. H. Telting[8], D. B. Guenther[9], T. Kallinger[10,5], R. Kuschnig[10,5], S. M. Rucinski[11], D. Sasselov[12], W. W. Weiss[10]

Draft version December 22, 2014

ABSTRACT

We present results from three weeks' photometric monitoring of the magnetic helium-strong star σ Ori E using the *MOST* microsatellite. The star's light curve is dominated by rotational modulation arising predominantly from plasma trapped in its co-rotating, centrifugally supported magnetosphere. The measured rotation period $P = 1.190847 \pm 0.000015$ d is consistent with the ephemeris published by Townsend et al. (2010), confirming that the star's rotation is steadily slowing due to magnetic braking. Analysis of the depths of light minima and the light-curve residuals fails to reveal any evidence for abrupt centrifugal breakout of plasma from the magnetosphere; together with a demonstration that the mass contained in the magnetosphere is significantly less than the theoretical asymptotic mass, these findings leads us to argue that breakout episodes do not play a significant role in establishing the star's magnetospheric mass budget.

Subject headings: stars: individual (HD 37479) — stars: magnetic fields — stars: rotation — stars: chemically peculiar — stars: early-type — circumstellar matter

1. INTRODUCTION

The B2Vpe star σ Ori E (HD 37479) is a magnetic helium-strong star characterized by variations in many of its observables, including photometric indices (Hesser et al. 1977), Hα emission (Reiners et al. 2000), UV wind absorption lines (Shore & Brown 1990), radio emission (Leone & Umana 1993), linear continuum polarization (Kemp & Herman 1977) and circular line polarization (Oksala et al. 2012). The 1.19 d period of these variations is identified with the star's rotation period, recently discovered to be gradually lengthening due to magnetic braking (Townsend et al. 2010, hereafter T10). The variability originates from a combination of surface abundance inhomogeneities and wind-originated plasma trapped in a circumstellar, co-rotating, centrifugally supported magnetosphere (Townsend et al. 2005, hereafter T05).

In this paper we present data from three weeks' photometric monitoring of σ Ori E by the *MOST* microsatellite (Walker et al. 2003), beginning November 2007. The original motivation behind this observing campaign was to better characterize the star's light curve, and to search for any cycle-to-cycle changes arising from the loss of magnetospheric plasma. The following section briefly reviews the physics underlying the magnetosphere of σ Ori E and related magnetic massive stars. Then, §3 describes the observations and explains the procedure used to reduce the raw data, and §4 analyzes various aspects of the light curve. The findings are discussed in §5 and then summarized in §6.

2. BACKGROUND

Magnetospheres around σ Ori E and other He-strong stars of recent interest (e.g., HR 7355 — Oksala et al. 2010; Rivinius et al. 2010, 2012; δ Ori C — Leone et al. 2010; HR 5907 — Grunhut et al. 2012) arise from the delicate interplay between magnetic fields, wind outflow and rapid rotation. Within the narrative of the *magnetically confined wind shock* (MCWS) paradigm proposed by Babel & Montmerle (1997b,a), radiation-driven wind streams originating from opposing footpoints of closed magnetic loops undergo head-on collisions near the loop summits. The wind plasma is shock-heated to millions of Kelvin and subsequently cools radiatively, initially by emission at X-ray wavelengths; this explains why a number of magnetic massive stars, including σ Ori E, are X-ray sources.

The fate of the cooled post-shock plasma is considered in the *rigidly-rotating magnetosphere* (RRM) model developed by Townsend & Owocki (2005). On sufficiently strong field loops the plasma is forced into co-rotation with the star. Outside the Kepler radius — the point where the local azimuthal velocity of the plasma matches

townsend@astro.wisc.edu
[1] Department of Astronomy, University of Wisconsin-Madison, 2535 Sterling Hall, 475 N. Charter Street, Madison, WI 53706, USA
[2] ESO - European Organisation for Astronomical Research in the Southern Hemisphere, Casilla 19001, Santiago 19, Chile
[3] NASA Ames Research Center, Moffett Field, CA 94035, USA
[4] Départment de physique, Université de Montréal C.P. 6128, Succursale Centre-Ville, Montréal, QC H3C 3J7, Canada
[5] Department of Physics and Astronomy, University of British Columbia, 6224 Agricultural Road, Vancouver, BC V6T 1Z1, Canada
[6] National Research Council of Canada, Herzberg Institue of Astrophysics, 5071 West Saanich Road, Victoria, BC, V9E 2E7, Canada
[7] LESIA, UMR 8109 du CNRS, Observatoire de Paris, UPMC, Université Paris Diderot, 5 place Jules Janssen, 92195, Meudon Cedex, France
[8] Nordic Optical Telescope, Apartado 474, 38700 Santa Cruze de La Palma, Spain
[9] Department of Astronomy and Physics, St. Marys University, Halifax, NS B3H 3C3, Canada
[10] University of Vienna, Institute for Astronomy, Türkenschanzstrasse 17, A-1180 Vienna, Austria
[11] Dept. of Astronomy and Astrophysics, University of Toronto, 50 St George Street, Toronto, ON M5S 3H4, Canada
[12] Harvard-Smithsonian Center for Astrophysics, 60 Garden Street, Cambridge, MA 02138, USA

the local orbital velocity — the centrifugal force exceeds the downward pull of gravity and can in principle support the plasma in magnetohydrostatic equilibrium for indefinite periods of time. Based on an empirical prescription for the wind mass flux at the footpoints of each closed loop, the RRM model predicts the relative density distribution of this centrifugally supported plasma throughout the magnetosphere. In the case of σ Ori E the predicted distribution consists primarily of a pair of circumstellar clouds situated at the intersections between magnetic and rotational equators, and these clouds are able successfully to reproduce key features of the star's Hα and photometric variability (see T05).

With continual wind feeding the total mass of plasma accumulated in a magnetosphere will grow with time, unless a countervailing mass leakage mechanism allows some kind of quasi-steady state to be reached. Townsend & Owocki (2005) propose a mechanism involving the stressing and eventual breaking of magnetic loops by the centrifugal force, which grows in strength as plasma accumulates. Magnetohydrodynamic (MHD) simulations by ud-Doula et al. (2006) support this *centrifugal breakout* hypothesis, and moreover suggest that the reconnection heating arising during breakout episodes could explain the X-ray flares seen in σ Ori E (over and above its quiescent MCWS-originated emission) by Groote & Schmitt (2004) and Sanz-Forcada et al. (2004). Cycle-to-cycle changes in the light curve might be expected from centrifugal breakout episodes; searching for these changes requires precise photometry over a long time series, a task well suited to *MOST*.

3. OBSERVATIONS AND DATA REDUCTION

3.1. *Overview*

MOST observed σ Ori E and four other bright B-type stars (HD 37525; σ Ori D; HD 37744; HD 294272) over the interval November 12 – December 3 2007 with a cadence of around 60 s. The telescope operated in direct imaging mode, where targets are placed on the open area of the science CCD not covered by the Fabry microlens array (see Rowe et al. 2006b,a); this comes at the cost of a degraded instrumental stability and precision, but is necessary because σ Ori E is too faint ($V = 6.66$) to observe in Fabry mode. Individual subexposures of 0.530 s were co-added onboard the satellite prior to downloading, to avoid saturating the telemetry link (see Rowe et al. 2008). The number of subexposures per co-added exposure was initially set at 31, but was then increased to 61 after the first 17 hours of the run.

At the beginning of the run σ Ori E fell outside the *MOST* continuous viewing zone (CVZ); therefore, for $\sim$ 25 minutes of every 101.413-minute orbit the satellite slewed to observe an alternative field in the Hyades, resulting in periodic gaps in the data (see Fig. 1). On November 23, σ Ori E entered the CVZ and *MOST* switched to observing the star continuously. Around half a day prior to this switch the onboard computer crashed, leading to a ~ 0.25 d gap in the data. The orientation of the spacecraft after the switch initially led to increased solar heating and a climb in the CCD temperature, accounting for certain features in the residual light curve (see §4.3). Finally, gaps in the data on December 2 and December 3 arose due to science data buffer overruns.

3.2. *Aperture Photometry*

The co-added exposures of σ Ori E, each a 20 by 20 pixel image, are reduced using the standard approach of synthetic aperture photometry. The stellar flux F_i is calculated as the difference between the total flux A_i in a 5-pixel radius circular aperture centered on the 2-dimensional Gaussian centroid of the image, and the imputed background flux B_i (arising primarily from stray light) in the same aperture,

$$F_i = A_i - B_i. \tag{1}$$

Here and throughout, the subscript $i = 1, \ldots, N$ is used to index exposures, with $N = 24\,455$ being the number of co-added exposures in the full run. The aperture flux is evaluated via

$$A_i = \frac{C_i}{\Delta t_i}, \tag{2}$$

where C_i is the measured number of counts in the aperture and Δt_i the exposure time. The units of A_i and other fluxes defined herein are counts per second.

3.3. *Background Flux Estimation*

The background flux B_i in eqn. (1) cannot be measured directly, but is customarily approximated using a 'sky' flux measured in a region surrounding the aperture. However, when applied to *MOST* direct imaging data this simple approach gives unsatisfactory results; although the background and sky fluxes are strongly correlated (see, e.g., Rowe et al. 2006a, their Fig. 3), the relationship between them is not completely linear. Such behavior is not wholly understood but likely stems from the complex spatial distribution of stray light falling on the detector, which varies on the satellite's orbital period (Reegen et al. 2006).

Accordingly, we determine the correlation between the background and sky fluxes empirically using an iterative procedure:

(i). Begin with the initial estimate

$$B_i = S_i,$$

where

$$S_i = \frac{n^A}{n^S}\,\frac{C_i^S}{\Delta t_i}$$

is the sky flux rescaled to the aperture size. Here, C_i^S is the number of counts measured in the sky region (defined by the non-aperture pixels), and n^S and n^A are the number of pixels composing the sky region and the aperture, respectively.

(ii). Calculate F_i from A_i and B_i via eqn. (1).

(iii). Decompose F_i into three components,

$$F_i = \overline{F} + \tilde{F}_i + \hat{F}_i,$$

with $\overline{F}$ being the weighted mean stellar flux, $\tilde{F}_i$ the periodic light variations due to rotational modulation, and $\hat{F}_i$ the residuals. The mean flux is calculated as

$$\overline{F} = \frac{\sum_{i=1}^N \varpi_i F_i}{\sum_{i=1}^N \varpi_i}.$$

where

$$\varpi_i = \frac{1}{\sigma_i^2}$$

is the weight of the i'th point in terms of its photometric (Poisson) error σ_i. Likewise, the periodic component is calculated as

$$\tilde{F}_i = \tilde{F}(\varphi_i),$$

where

$$\varphi_i \equiv \nu t_i$$

is the rotation phase of the i'th exposure, t_i is the corresponding mid-exposure time, ν is the rotation frequency of the star, and the 'periodic flux function' $\tilde{F}(\varphi)$ repeats on the interval $0 \leq \varphi \leq 1$. The construction of this function is discussed in §3.5.

(iv). Calculate the total aperture flux pre-whitened by the mean and periodic signals,

$$\hat{A}_i = A_i - \overline{F} - \tilde{F}_i = \hat{F}_i + B_i$$

(v). Update the background flux as

$$B_i = B(S_i),$$

where the 'background flux function' $B(S)$ comes from a smooth fit to the $(S_i, \hat{A}_i)$ points. The construction of this function is discussed in §3.4.

(vi). If the maximal relative change in B_i from the preceding iteration, across all i, remains above some threshold (taken throughout to be 10^{-3}), go back to step (ii); otherwise, the procedure is complete.

The pre-whitening in step (iv) is necessary because the periodic variations $\tilde{F}_i$ are *not* correlated with S_i, and will distort the fit in step (v) unless removed.

3.4. *Background Flux Function*

The background flux function $B(S)$ is determined via a smooth fit to the $(S_i, \hat{A}_i)$ data using the locally weighted regression algorithm devised by Cleveland (1979). In brief, the function at any S (not necessarily equal to the observed abscissae S_i) is calculated via a linear least-squares fit to the data using weights which filter out all but the r points closest to S. The weights are usually based on a tri-cubed function (Cleveland 1979); however, we choose to introduce additional weighting based on the photometric errors. The overall weighting of the i'th point in the least-squares fit is thus defined as

$$w_i = \begin{cases} \left(1 - \left|\frac{S_i - S}{h}\right|^3\right)^3 \varpi_i & \text{if } |S_i - S| < h, \\ 0 & \text{otherwise.} \end{cases} \quad (3)$$

The smoothing length h is set equal to the absolute separation $|S_r - S|$ of the r'th closest point to S. A global smoothing parameter $0 < f \leq 1$ is used to set r as the smallest integer greater than or equal to the product fN. The choice of f is discussed in §3.6.

3.5. *Periodic Flux Function*

To determine the periodic flux function $\tilde{F}(\varphi)$ we apply the same locally weighted regression algorithm described above to the $(\varphi_i, F_i - \overline{F})$ data. Weights are calculated similarly to eqn. (3), but periodic boundary conditions are applied when evaluating the absolute separations $|\varphi_r - \varphi|$. The parameter r is set using a global smoothing parameter $\tilde{f}$, defined in the same way as f above; the choice of $\tilde{f}$ is discussed in §3.6.

To allow an independent determination of the star's rotation period (§4.2), the frequency ν is not specified *a priori* but rather chosen to minimize the weighted mean square error

$$\epsilon(\tilde{F}) = \frac{\sum_{i=1}^{N} \varpi_i [F_i - \overline{F} - \tilde{F}(\varphi_i)]^2}{\sum_{i=1}^{N} \varpi_i}. \quad (4)$$

This period-search approach is similar to the popular phase dispersion minimization (PDM) algorithm introduced by Stellingwerf (1978).

3.6. *Selection of Smoothing Parameters*

The fitting procedures described in §§3.4 and 3.5 both use the locally weighted regression algorithm. To select appropriate values for the global smoothing parameters $(f, \tilde{f})$ we use K-fold cross validation (CV), a well-established technique in the statistical community (see Arlot & Celisse 2010, for a review) which is seeing increasing application in astrophysical contexts, especially for automated classification (e.g., de la Calleja & Fuentes 2004; Feeney et al. 2005; Blondin et al. 2011).

The observational data are randomly partitioned into K approximately equal-sized sets. For a given $(f, \tilde{f})$ the reduction procedure is applied to the data comprising $K-1$ of the sets taken together (the 'training' set), with the remaining set (the 'validation' set) put aside. The locally weighted regression fits to the background flux and periodic stellar flux, together with the mean flux, are used to calculate the synthetic aperture flux

$$\mathcal{A}(S, \varphi) = \overline{F} + B(S) + \tilde{F}(\varphi). \quad (5)$$

The 'predictivity' of the data reduction — how well it can model the behavior of the validation set, despite being based on the training set — is then quantified via the weighted mean square error

$$\epsilon(\mathcal{A}) = \frac{\sum_{i=1}^{N} \mu_i \varpi_i [A_i - \mathcal{A}(S_i, \varphi_i)]^2}{\sum_{i=1}^{N} \mu_i \varpi_i}. \quad (6)$$

Here, the mask μ_i is equal to 1 if the i'th point is in the validation set, and 0 otherwise.

This procedure is repeated K times, with each set in turn serving as the validation set while the remainder are used to form the training set. The arithmetic mean of the resulting K values of $\epsilon(\mathcal{A})$ is adopted as a measure of the predictivity of the data reduction for the chosen $(f, \tilde{f})$ pair. To find the optimal combination of these parameters, we search over the ranges $-2 \leq \log_{10} f \leq -0.3$ and $-2.5 \leq \log_{10} \tilde{f} \leq -1$ for the combination which minimizes the mean $\epsilon(\mathcal{A})$. For a partition factor $K = 10$, the minimum occurs at $(f, \tilde{f}) = (0.084, 0.019)$, and we

adopt these parameters throughout (similar values result from choosing $K = 5$ or $K = 20$).

4. ANALYSIS

The ultimate outcome of the data reduction process is presented in Fig. 1, which plots the stellar flux in magnitudes relative to the mean flux,

$$m = -2.5 \log \left(\frac{F}{\overline{F}} \right), \tag{7}$$

as a function of time. The following sections explore various aspects of this light curve.

4.1. *Periodic Variations*

The periodic component of the stellar flux, defined in magnitudes as

$$\tilde{m} = -2.5 \log \left(1 + \frac{\tilde{F}}{\overline{F}} \right), \tag{8}$$

is plotted over the light curve in Fig. 1. It clearly highlights the signature twice-per-rotation eclipse-like dimmings of the star first revealed in full by Hesser et al. (1976). As discussed by T05 and Townsend (2008), these light minima arise when the two principal magnetospheric clouds (see §2) transit across and occult the stellar disk. In contrast to the narrow, symmetric primary (deeper) minimum, the secondary minimum is broad, shallow, and shows a distinct asymmetry. This asymmetry, which can also be seen in the earlier photometry by Hesser et al. (1977) and Oksala & Townsend (2007), suggests that the cloud responsible for the secondary minimum is itself divided into two smaller subclouds, with the trailing one containing more mass than the leading one (see also Smith & Bohlender 2007).

T05 attribute the brightening seen after the secondary eclipse to photospheric flux variations arising from the inhomogeneous surface abundance distribution. We briefly discuss future prospects for modeling these variations in §5.

4.2. *Period Measurement*

The rotation frequency found by minimizing $\epsilon(\tilde{F})$ is $\nu = 0.839739 \pm 0.000010\,\mathrm{d}^{-1}$, which corresponds to a rotation period $P = 1.190847 \pm 0.000015\,\mathrm{d}$. The quoted uncertainties are calculated using bootstrap Monte-Carlo simulations (e.g., Press et al. 1992). Random sampling with replacement is applied to the $(\varphi_i, F_i - \overline{F})$ data, to construct 10^7 synthetic light curves; for each of these ν is determined as before by minimizing $\epsilon(\tilde{F})$. Fig. 2 plots the probability distribution function $\mathrm{d}p/\mathrm{d}P$ of the resulting synthetic rotation periods. The shaded region is constructed to be symmetric about the measured period and enclose 68.2%[13] of the area under the curve. The width of this region is $\pm 0.000015\,\mathrm{d}$, which is the basis for the quoted uncertainty in P.

The ephemeris constructed by T10, which accounts for the braking of the star's rotation, predicts an instantaneous period $P = 1.190851 \pm 0.000003\,\mathrm{d}$ at the time of the *MOST* observations; as illustrated in Fig. 2 this is in excellent agreement with the period reported here. A further check on the ephemeris comes from comparing t_o and t_c, the observed and calculated (T10, their eqn. 5) times of primary minima in the light curve, respectively. Table 1 summarizes these timing data, with the t_o values measured using the parabolic minimum fitting described by T10. The calculated times clearly lag the observed times, with the difference $t_\mathrm{o} - t_\mathrm{c}$ having a mean $-0.0057\,\mathrm{d}$ and a scatter wholly consistent with the tabulated t_o measurement errors. This lag may arise from the uncertainties in the ephemeris, but it could also be a manifestation of the wavelength-dependent timing effects discussed in §3.4 of T10, because the *MOST* passband (see Walker et al. 2003, their Fig. 4) is redder than the Johnson U passband used in the T10 observations. Either way, however, the lag amounts to only ~ 0.005 of the rotation period; and therefore this good agreement between observed and calculated minima times serves as additional, strong confirmation of the T10 ephemeris.

E	t_o (HJD)	t_c (HJD)	$t_\mathrm{o} - t_\mathrm{c}$ (d)
9774	2454418.0657 ± 0.0009	2454418.070	-0.0044
9775	2454419.2553 ± 0.0006	2454419.261	-0.0056
9776	2454420.4467 ± 0.0008	2454420.452	-0.0051
9777	2454421.6375 ± 0.0008	2454421.643	-0.0051
9778	2454422.8282 ± 0.0007	2454422.833	-0.0053
9779	2454424.0195 ± 0.0009	2454424.024	-0.0048
9780	2454425.2081 ± 0.0008	2454425.215	-0.0071
9781	2454426.3984 ± 0.0007	2454426.406	-0.0076
9782	2454427.5920 ± 0.0006	2454427.597	-0.0049
9783	2454428.7825 ± 0.0009	2454428.788	-0.0052
9784	2454429.9728 ± 0.0009	2454429.979	-0.0058
9785	2454431.1638 ± 0.0010	2454431.169	-0.0057
9786	2454432.3544 ± 0.0009	2454432.360	-0.0059
9787	2454433.5453 ± 0.0010	2454433.551	-0.0058
9788	2454434.7355 ± 0.0010	2454434.742	-0.0065
9789	2454435.9276 ± 0.0008	2454435.933	-0.0053
9790	2454437.1165 ± 0.0007	2454437.124	-0.0071

TABLE 1
Observed (t_o) and predicted (t_c) times of primary light minima, labeled by their cycle number E (see T10), together with their differences.

4.3. *Residual Flux*

Figure 3 plots the residual component of the stellar flux, defined in magnitudes as

$$\hat{m} = -2.5 \log \left(1 + \frac{\hat{F}}{\overline{F}} \right). \tag{9}$$

A $\pm 0.1\,\mathrm{d}$ boxcar mean curve, together with the associated one-standard-deviation bounds, is plotted below the points to highlight long-term trends in the data. This smoothed curve clearly reveals an abrupt dimming by about 0.0035 mag near the mid-point of the observations ($t - 2454416.5 \approx 11$), together with a reduction in the standard deviation. Also visible in the curve is a low-level ripple with a frequency $\sim 1 - 2\,\mathrm{d}^{-1}$. However, the corresponding smoothed light curve of HD 37744 (also shown in the figure) reveals similar behavior in both respects; hence, neither the dimming nor the ripple can be intrinsic to σ Ori E. The effects are likely instrumental in origin; the dimming in particular is correlated with a

[13] Chosen as the extent of the 1-σ confidence interval for a Gaussian distribution; but note that the distribution shown in Fig. 2 is only approximately Gaussian.

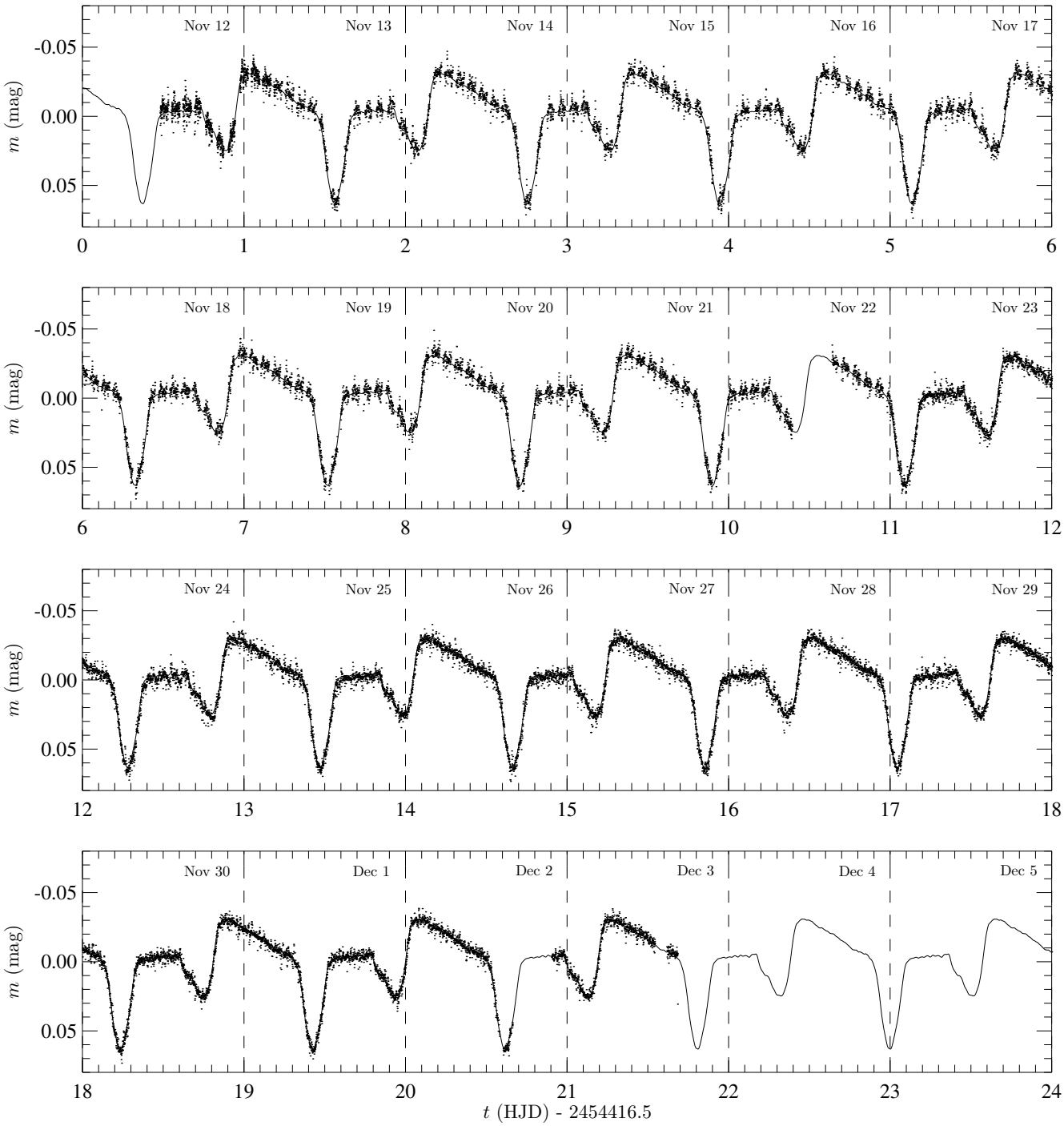

FIG. 1.— The stellar flux m in magnitudes relative to the mean flux, plotted as a function of time. The solid curve overlaying the data shows the periodic component $\tilde{m}$. The vertical dashed lines delineate the day boundaries.

sharp 5 K increase in the temperature of the CCD preamplifier, due to the increased solar heating which occurred when *MOST* switched to continuous observation of σ Ori E (cf. §3.1).

Apart from these instrumental variations, the smoothed curve in Fig. 3 is relatively devoid of features. In particular, there are no obvious flares characterized by a sudden brightening of the star followed by a slow decline. One interpretation of this result is that there were no centrifugal breakout episodes during the *MOST* run, since any breakout would be accompanied by a large release of magnetic energy. A caveat, however, is that although a link between magnetic reconnection and optical flaring has been established in other types of system (e.g., weak-line T Tauri stars — Fernández et al. 2004; M dwarfs — Stelzer et al. 2006), the same cannot be said for the centrifugally supported magnetospheres considered here. The MHD breakout simulations by ud-Doula et al. (2006) cannot offer much guidance, since they lack the necessary microphysics to determine the energy yield

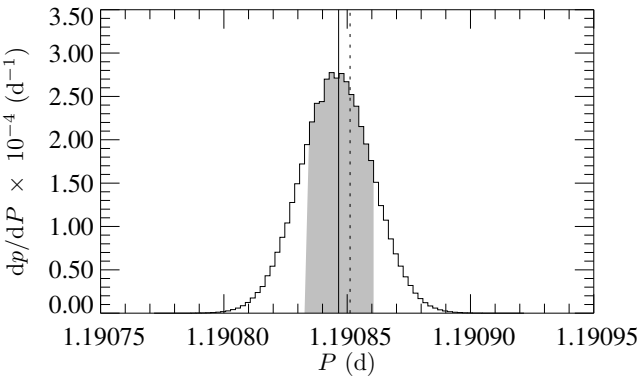

FIG. 2.— The probability distribution function of synthetic rotation periods obtained from the Monte-Carlo simulation. The shaded region is centered on the measured period $P = 1.190847\,\mathrm{d}$ (shown as the solid vertical line) and encloses 68.2 % of the area under the curve. The instantaneous period $P = 1.190851$ calculated using the T10 ephemeris is shown as the dotted vertical line.

across the electromagnetic spectrum.

To uncover any low-amplitude periodic signals present in the residual flux, Fig. 4 plots the Lomb-Scargle periodogram $\mathcal{P}(\nu)$ of $\hat{F}$ for frequencies extending up to $100\,\mathrm{d}^{-1}$. Also shown is the critical threshold $\mathcal{P}_\mathrm{c} = 13.1$ corresponding to a false-alarm probability $p(\mathcal{P} > \mathcal{P}_\mathrm{c}) = 0.05$ (see Press et al. 1992, their §13.8). Peaks rising above this threshold can be seen at $\nu = 14.2\,\mathrm{d}^{-1}$ and its harmonics, along with $\pm 1, 2, 3, \ldots\ \mathrm{d}^{-1}$ beat frequencies. Recognizing the $14.2\,\mathrm{d}^{-1}$ signal as the orbital frequency of *MOST*, these peaks can be attributed to the gaps in the data for the first half of the observing, and/or imperfect subtraction of the background flux. The beat frequencies arise because the Earthshine contribution to the stray light (primarily from the high-albedo polar regions) are modulated on a 1-day period (Reegen et al. 2006). We note that if we bypass the iterative background flux estimation procedure described in §3.3, and instead assume $B_i = S_i$, then the periodogram peaks discussed here are a factor-10 higher. This serves as *a posteriori* justification for adopting the iterative procedure, even though it is more complex and time-consuming.

The periodogram also reveals power at $\sim 1\,\mathrm{d}^{-1}$ and $\sim 2\,\mathrm{d}^{-1}$ due to the instrumental ripple, and at low frequencies ($< 1\,\mathrm{d}^{-1}$) presumably due to the instrumental dimming. However, no other peaks rise above the false-alarm threshold $\mathcal{P}_\mathrm{c}$, strongly suggesting that σ Ori E exhibits no periodic light variations other than the rotational modulation.

4.4. *Magnetospheric Evolution*

To examine any changes in the magnetospheric mass during the observing run (as expected, for instance, due to centrifugal breakout episodes), Fig. 5 plots the relative depths of the primary and secondary minima as a function of time. These are defined as

$$\Delta m_\mathrm{p} = m_\mathrm{p} - m_\mathrm{b}, \qquad \Delta m_\mathrm{s} = m_\mathrm{s} - m_\mathrm{b}, \tag{10}$$

respectively, where m_p and m_s are the stellar flux in magnitudes at the primary and secondary light minima, determined from the parabolic fitting discussed in Section 4.2; while m_b is the mean flux between each pair of minima, averaged over the phase interval 0.15 – 0.25. Although the figure reveals changes in Δm_p and Δm_s at a level $\sim 0.002\,\mathrm{mag}$ which exceeds the error bars, there are no abrupt and ongoing reductions in the depths which might signify the loss of material from the magnetospheric clouds. Indeed, the changes appear more consistent with the instrumental variations mentioned in the previous section.

M_* ($\mathrm{M}_\odot$)	R_* ($\mathrm{R}_\odot$)	Ω (Ω_c)	B_* (kG)	β (°)	ϵ_*
8.30	3.77	0.454	11.0	55	10^{-3}

TABLE 2
PARAMETERS ADOPTED IN CALCULATING THE INFERRED MAGNETOSPHERE MASS M_mag AND ASYMPTOTIC MAGNETOSPHERE MASS M_∞ OF σ ORI E.

5. DISCUSSION

An important outcome from the *MOST* observations is the measurement of the rotation period of σ Ori E with a precision sufficient to test the T10 ephemeris. The good agreement found between observed and calculated periods, and likewise for the timing of the light minima, validates the ephemeris and moreover confirms that the magnetic braking of σ Ori E is steady rather than episodic. This is in contrast to the 'glitchy' spindown seen in some Ap stars (e.g., CU Vir; see Mikulášek et al. 2011, and references therein), but agrees with the MHD simulations by ud-Doula et al. (2009) which suggest that angular momentum loss from massive-star magnetospheres is a smooth process.

Another noteworthy result is the failure to find any evidence for centrifugal breakout episodes, either in the form of optical flares in the residual flux (§4.3) or as systematic reductions in the depths of the light minima (§4.4). This could be due simply to unlucky scheduling of the *MOST* run, coupled with the fact that the breakout recurrence timescale is poorly constrained (as it depends on the unknown wind mass-loss rate). However, there are a number of independent arguments which favor the alternative conclusion that centrifugal breakout simply *does not occur* in σ Ori E, at least at a level where it has any impact on the magnetospheric mass budget.

Foremost amongst these is the discrepancy between the magnetospheric mass M_mag inferred from the observations together with the RRM model, and the asymptotic magnetosphere mass M_∞ predicted by the breakout analysis of Townsend & Owocki (2005, their Appendix A2); if centrifugal breakout plays a role in governing the magnetospheric mass budget, then these two values should be comparable. Table 2 lists the stellar and magnetosphere parameters adopted here to evaluate M_mag and M_∞; the field strength B_*, magnetic obliquity β and magnetosphere scale-height parameter ϵ_* are taken from T05, while the other parameters are derived in Appendix A. Applying the light-curve synthesis procedure described by T05, the RRM model requires $\rho_\mathrm{max}\kappa R \approx 7$ to reproduce the observed depth $\Delta m_\mathrm{p} \approx 0.065$ of the primarily light minima (cf. Fig. 5), with ρ_max being the maximum mass density in the magnetosphere, κ the flux-mean opacity in the *MOST* passband, and R the stellar radius. A lower limit on the opacity is given by the electron scattering value, $\kappa_\mathrm{es} = 0.34\,\mathrm{cm}^2\,\mathrm{g}^{-1}$ for a fully ionized solar-abundance composition. With $R = 3.77\,\mathrm{R}_\odot$ from Table 2, we therefore obtain an upper

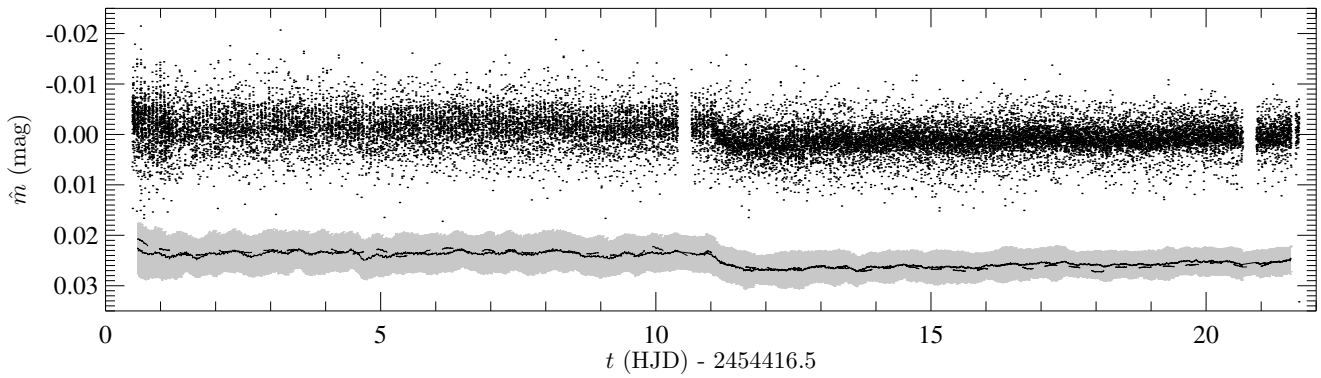

FIG. 3.— The residual stellar flux $\hat{m}$ in magnitudes relative to the mean flux, plotted as a function of time. The solid curve beneath (shifted down by 0.025 mag for clarity) shows the ± 0.1 d boxcar mean curve, with the gray envelope illustrating the associated one-standard-deviation bounds. For comparison, the dashed curve shows the corresponding smoothed light curve of HD 37744.

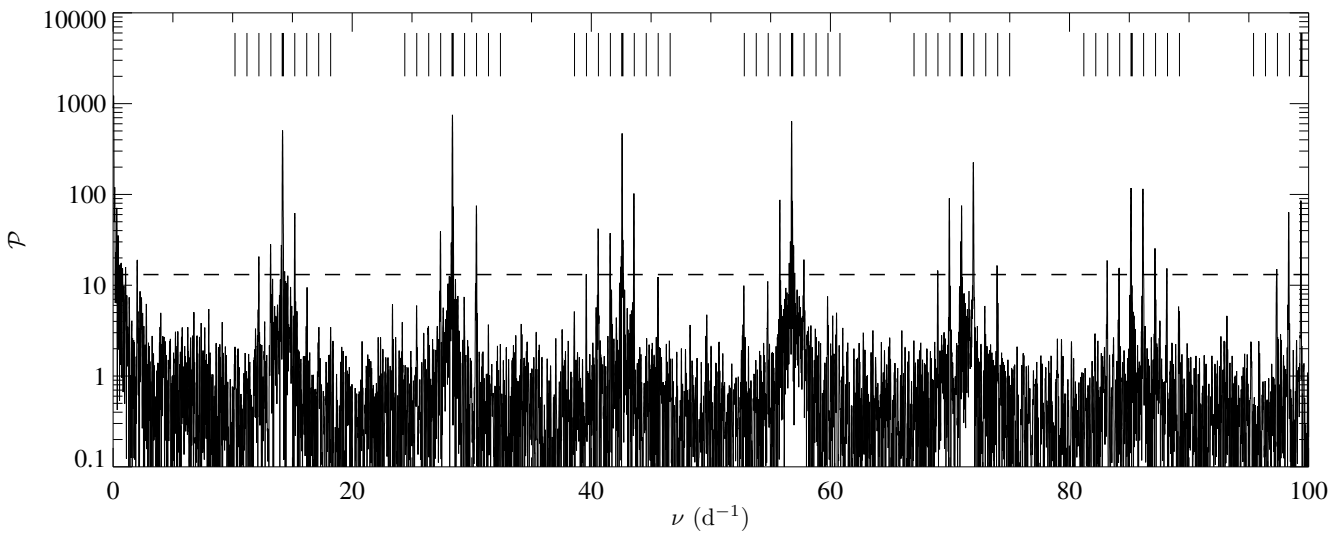

FIG. 4.— The Lomb-Scargle periodogram $\mathcal{P}$ of the residual flux $\hat{F}$, plotted as a function of frequency ν. Vertical tick marks indicate the $14.2\,\mathrm{d}^{-1}$ orbital signal and its harmonics (thick) and the $1\,\mathrm{d}^{-1}$ aliases of these peaks (thin). The horizontal dashed line indicates the $\mathcal{P}_\mathrm{c} = 13.1$ threshold corresponding to a false-alarm probability $p(\mathcal{P} > \mathcal{P}_\mathrm{c}) = 0.05$.

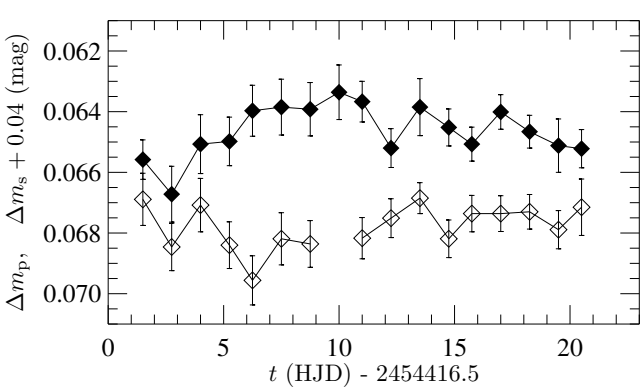

FIG. 5.— Depths of primary (Δm_p; filled symbols) and secondary (Δm_s; open symbols) light minima, plotted in magnitudes as a function of time. The Δm_s data have been shifted vertically to facilitate comparison between the two; the missing data point comes from the corresponding gap in the light curve on November 22 (cf. Fig. 1).

limit $\rho_\mathrm{max} \lesssim 8\times10^{-11}\,\mathrm{g\,cm^{-3}}$ on the maximum density[14]. Integrating over the RRM density distribution leads to a corresponding upper mass limit $M_\mathrm{mag} \lesssim 2 \times 10^{-10}\,\mathrm{M}_\odot$. This is almost two orders of magnitude smaller than the asymptotic mass $M_\infty = 1.2 \times 10^{-8}\,\mathrm{M}_\odot$ predicted by the breakout analysis, indicating that the magnetosphere is well short of the level required for significant breakout episodes to occur.

Further corroborating arguments are presented in a forthcoming paper (Townsend et al., in preparation), which demonstrates that the low-mass companion discovered by Bouy et al. (2009) is responsible for 70% of the X-ray flux from the σ Ori E system. It seems likely that the X-ray flares believed originally to arise during centrifugal breakout (see §2) instead come from the magnetic activity of the companion.

These findings are significant because they challenge

[14] This is a very conservative estimate; using the Inglis-Teller effect, both Groote & Hunger (1982) and Smith & Bohlender (2007) derive a bound $n_\mathrm{e} \lesssim 2\times10^{12}\,\mathrm{cm^{-3}}$ on the electron number density, which corresponds to the tighter upper limit $\rho \lesssim 4\times10^{-12}\,\mathrm{g\,cm^{-3}}$.

the prevailing narrative for mass leakage from centrifugally supported magnetospheres. It is natural to now ask what other leakage mechanism(s) might be at work to balance the continual feeding of plasma from the wind, as evidenced by the star's rotationally modulated UV absorption lines (Shore & Brown 1990). Havnes & Goertz (1984) explore cross-field diffusive processes such as ambipolar diffusion, but find them far too slow to be effective; revisiting their calculations with updated stellar parameters does not change this conclusion. A related question concerns the process(es) responsible for magnetospheric features not predicted by the RRM model — for instance, the subclouds seen in the secondary light minima (cf. Fig. 1). Corresponding departures from the RRM model have been noted in a number of other He-strong stars harboring magnetospheres (in particular, those mentioned in §2). Are these a consequence of the as-yet-unidentified mass-leakage mechanism, or instead due to departures from a pure-dipole field topology? In the case of σ Ori E, recent spectropolarimetric measurements by Oksala et al. (2012) indeed reveal departures from dipolarity, although these are not consistent with the decentered dipole invoked by T05 to explain the overall difference in the depths of the primary and secondary light minima. Clearly, there remains much work to be done in understanding the effects of mass redistribution, mass leakage and field topology in governing the distribution and overall amount of plasma in these stars' magnetospheres.

Looking now to the future, a logical next step is to decompose the *MOST* light curve into magnetospheric and photospheric components. This will allow quantitative testing of the assumption (see §4.1) that the brightening after the secondary light minimum is due to the star's inhomogeneous surface abundance distribution. For other He-strong stars Krtička et al. (2007, 2011) have successfully used surface abundance maps derived from Doppler imaging to reproduce the stars' light variations. With abundance maps now becoming available for σ Ori E (see Oksala et al. 2012), it should be possible to apply the same technique to disentangle the magnetospheric and photospheric components of the light curve. The magnetospheric component can then be compared against the light-curve morphologies predicted by the RRM model (see Townsend 2008); with a good match between theory and observation, further constraints can be placed on parameters such as the stellar inclination, magnetic obliquity and magnetospheric mass.

6. SUMMARY

We have undertaken a careful reduction and analysis of the *MOST* observations of σ Ori E. A key result is that the *MOST* data provide independent confirmation (§4.2) of the ephemeris published by Townsend et al. (2010), confirming that magnetic braking is occurring in σ Ori E and that this braking is a steady process.

An equally important result is the absence of any evidence for centrifugal breakout episodes, either in the residual flux (§4.3) or in the depths of the primary light minima (§4.4). Moreover, the observationally inferred magnetospheric mass (§5) is around two orders of magnitude below the asymptotic mass predicted by the breakout analysis of Townsend & Owocki (2005). These findings lead us to rule out centrifugal breakout as a mechanism for magnetospheric mass leakage in σ Ori E.

RHDT acknowledges support from NSF awards AST-0908688 and AST-0904607, and NASA award NNX12AC72G. AFJM, DBG, JMM and SMR are grateful for financial support from NSERC (Canada).

APPENDIX

FUNDAMENTAL PARAMETERS OF σ ORI E

Groote & Hunger (1982) determine an effective temperature $T_{\rm eff} = 22\,500\,{\rm K}$ for σ Ori E by fitting the spectral energy distribution from UV through to IR. They likewise derive a surface gravity $\log g = 3.85\,{\rm dex}$ from modeling H and He equivalent widths. A subsequent more-detailed analysis of Balmer-line wings led Hunger et al. (1989) to revise this value slightly upwards, to $\log g = 3.95\,{\rm dex}$. As discussed by these latter authors, the $T_{\rm eff}$ and $\log g$ together imply that σ Ori E is more distant ($\sim 650\,{\rm pc}$) than the σ Ori cluster ($\sim 450\,{\rm pc}$), and is moreover a factor ~ 10 older than the cluster. These findings, however, stand contrary to a number of observational results indicating that σ Ori E is a bona fide member of the cluster rather than a background star. The reddening of σ Ori E is the same as σ Ori AB (Sherry et al. 2008), and likewise for interstellar polarization (Kemp & Herman 1977). The radial velocity and proper motion of σ Ori E are indistinguishable from those of the cluster (Caballero 2007). Finally, the spindown measurements by T10 indicate that the star is young, with an age $\sim 1.1\,{\rm Myr}$ consistent with lower-end age estimates for the cluster.

The problem with the Hunger et al. (1989) analysis likely resides in the surface gravity determination. Emission from magnetospheric plasma fills in the wings of Balmer lines; if not properly corrected this makes the lines appear less broad, and the gravity consequently smaller, than is actually the case. Given this complication it seems better to avoid the gravity measurement altogether, and derive stellar parameters using a different approach. Accordingly, assuming σ Ori E is a cluster member, a radius $R = 3.77\,{\rm R}_\odot$ follows from the angular diameter $\theta = 0.079\,{\rm mas}$ (Groote & Hunger 1982) and the cluster distance $d = 444\,{\rm pc}$ derived for solar metallicity by Sherry et al. (2008).

To obtain the corresponding mass, we calculate a sequence of solar-metallicity evolutionary tracks with masses $M = 7, 7.1, 7.2, \ldots, 9.9, 10\,{\rm M}_\odot$ using the MESA stellar evolution code (Paxton et al. 2011). For simplicity the calculations neglect the effects of rotation. The $M = 8.3\,{\rm M}_\odot$ track passes closest to $T_{\rm eff} = 22\,500\,{\rm K}$, $R = 3.77\,{\rm R}_\odot$ point, and we adopt this as the stellar mass. With the observed rotation period (§4.2) the dimensionless angular velocity is $\omega = \Omega/\Omega_{\rm c} = 0.454$, where $\Omega \equiv 2\pi\nu$ and $\Omega_{\rm c} = \sqrt{8GM/27R^3}$ is the critical angular velocity.

REFERENCES

Arlot, S., & Celisse, A. 2010, Statistics Surveys, 4, 40

Babel, J., & Montmerle, T. 1997a, ApJ, 485, L29

—. 1997b, A&A, 323, 121
Blondin, S., Mandel, K. S., & Kirshner, R. P. 2011, A&A, 526, A81
Bouy, H., Huélamo, N., Martín, E. L., et al. 2009, A&A, 493, 931
Caballero, J. A. 2007, A&A, 466, 917
Cleveland, W. S. 1979, J. American Statistical Association, 74, 829
de la Calleja, J., & Fuentes, O. 2004, MNRAS, 349, 87
Feeney, S. M., Belokurov, V., Evans, N. W., et al. 2005, AJ, 130, 84
Fernández, M., Stelzer, B., Henden, A., et al. 2004, A&A, 427, 263
Groote, D., & Hunger, K. 1982, A&A, 116, 64
Groote, D., & Schmitt, J. H. M. M. 2004, A&A, 418, 235
Grunhut, J. H., Rivinius, T., Wade, G. A., et al. 2012, MNRAS, 419, 1610
Havnes, O., & Goertz, C. K. 1984, A&A, 138, 421
Hesser, J. E., Ugarte, P. P., & Moreno, H. 1977, ApJ, 216, L31
Hesser, J. E., Walborn, N. R., & Ugarte, P. P. 1976, Nature, 262, 116
Hunger, K., Heber, U., & Groote, D. 1989, A&A, 224, 57
Kemp, J. C., & Herman, L. C. 1977, ApJ, 218, 770
Krtička, J., Marková, H., Mikulášek, Z., et al. 2011, in IAU Symposium, Vol. 272, Active OB Stars: Mass-Loss, Rotation and Critical Limits, ed. C. Neiner, G. Wade, G. Meynet, & G. Peters, 517
Krtička, J., Mikulášek, Z., Zverko, J., & Žižňovský, J. 2007, A&A, 470, 1089
Leone, F., Bohlender, D. A., Bolton, C. T., et al. 2010, MNRAS, 401, 2739
Leone, F., & Umana, G. 1993, A&A, 268, 667
Mikulášek, Z., Krtička, J., Janík, J., et al. 2011, in Magnetic Stars, ed. I. I. Romanyuk & D. O. Kudryavtsev, 52
Oksala, M., & Townsend, R. H. D. 2007, in ASP Conference Series, Vol. 361, Active OB-Stars: Laboratories for Stellare and Circumstellar Physics, ed. A. T. Okazaki, S. P. Owocki, & S. Štefl, 476
Oksala, M. E., Wade, G. A., Marcolino, W. L. F., et al. 2010, MNRAS, 405, L51
Oksala, M. E., Wade, G. A., Townsend, R. H. D., et al. 2012, MNRAS, 419, 959
Paxton, B., Bildsten, L., Dotter, A., et al. 2011, ApJS, 192, 3
Press, W. H., Teukolsky, S. A., Vetterling, W. T., & Flannery, B. P. 1992, Numerical recipes in FORTRAN, 2nd edn. (Cambridge University Press, Cambridge UK)
Reegen, P., Kallinger, T., Frast, D., et al. 2006, MNRAS, 367, 1417
Reiners, A., Stahl, O., Wolf, B., Kaufer, A., & Rivinius, T. 2000, A&A, 363, 585
Rivinius, T., Szeifert, T., Barrera, L., et al. 2010, MNRAS, 405, L46
Rivinius, T., Townsend, R. H. D., Kochukhov, O., et al. 2012, MNRAS, submitted
Rowe, J. F., Matthews, J. M., Seager, S., et al. 2006a, ApJ, 646, 1241
Rowe, J. F., Matthews, J. M., Kuschnig, R., et al. 2006b, Mem. Soc. Astron. Italiana, 77, 282
Rowe, J. F., Matthews, J. M., Seager, S., et al. 2008, ApJ, 689, 1345
Sanz-Forcada, J., Franciosini, E., & Pallavicini, R. 2004, A&A, 421, 715
Sherry, W. H., Walter, F. M., Wolk, S. J., & Adams, N. R. 2008, AJ, 135, 1616
Shore, S. N., & Brown, D. N. 1990, ApJ, 365, 665
Smith, M. A., & Bohlender, D. A. 2007, A&A, 475, 1027
Stellingwerf, R. F. 1978, ApJ, 224, 953
Stelzer, B., Schmitt, J. H. M. M., Micela, G., & Liefke, C. 2006, A&A, 460, L35
Townsend, R. H. D. 2008, MNRAS, 389, 559
Townsend, R. H. D., Oksala, M. E., Cohen, D. H., Owocki, S. P., & ud-Doula, A. 2010, ApJ, 714, L318, (T10)
Townsend, R. H. D., & Owocki, S. P. 2005, MNRAS, 357, 251
Townsend, R. H. D., Owocki, S. P., & Groote, D. 2005, ApJ, 630, L81, (T05)
ud-Doula, A., Owocki, S. P., & Townsend, R. H. D. 2009, MNRAS, 392, 1022
ud-Doula, A., Townsend, R. H. D., & Owocki, S. P. 2006, ApJ, 640, L191
Walker, G., Matthews, J., Kuschnig, R., et al. 2003, PASP, 115, 1023